

## Regime Transitions in a Stochastically Forced Double-Gyre Model

PHILIP SURA, KLAUS FRAEDRICH, AND FRANK LUNKEIT

*Meteorologisches Institut der Universität Hamburg, Hamburg, Germany*

(Manuscript received 2 September 1999, in final form 28 March 2000)

### ABSTRACT

A reduced-gravity double-gyre ocean model is used to study the influence of an additive stochastic wind stress component on the regime behavior of the wind-driven circulation. The variance of the stochastic component (spatially coherent white noise) representing the effect of atmospheric transient eddies is chosen to be spatially inhomogeneous. This is done to account for the observed concentration of eddy activity along the North Atlantic and North Pacific storm tracks. As a result the double-gyre model with a spatially inhomogeneous stochastic forcing shows a bimodal behavior. One regime shows a quasi-antisymmetric; the second regime a nonsymmetric flow pattern. It is suggested that the nonsymmetric regime corresponds to one member of a known nonsymmetric pair of stationary solutions. Actually no stationary solutions are explicitly calculated in this study. The bimodality does not appear without a spatially inhomogeneous stochastic forcing nor with spatially homogeneous stochastic forcing. Therefore, the regime transitions are induced by the inhomogeneity of the white noise variance. The study suggests that the stochastic forcing enables the system to reach the neighborhood of an unstable fixed point that is not reached without the spatially inhomogeneous stochastic wind field. The unstable fixed point then acts to steer the model in a temporarily persistent regime.

### 1. Introduction

Prototypes for the study of the midlatitude wind-driven ocean circulation are the single-gyre and double-gyre models in a rectangular basin. They are designed as conceptual tools to study physical mechanisms and are hardly used to simulate the actual ocean circulation. The solutions depend sensitively on boundary conditions and subgrid-scale parameterizations that are poorly known from observations. Therefore, one of the main tasks of the wind-driven single or double gyre is to explore the role of dissipative processes within the western boundary currents [for a review see Pedlosky (1996)]. The role played by dissipative processes to balance the continuous input of vorticity by the wind stress is not the only fundamental problem analyzed by the wind-driven gyre models. Their rich structure of multiple equilibria is becoming evident. In particular, the dynamics of the double-gyre flow has received considerable attention as a conceptual model for the North Atlantic current system.

For explaining climate variability, large-scale atmospheric and oceanic multiple equilibria play a viable role. Only those steady states that are stable can be reached by a time stepping procedure. However, steady

states that are unstable to a small number of modes, but stable to a large number of modes, may act to steer a time-dependent model, thus providing a mechanism for a temporarily persistent regime (Legras and Ghil 1985). Regimes are defined as regions in the systems phase space where the probability of occurrence attains local maxima. The definition is due to the fact that a chaotic system may possess a set of attractor basins each much smaller than the phase space of the entire system.

Atmospheric low-frequency variability has been associated with the irregular transition among weather regimes (Kimoto and Ghil 1993a,b; Itoh and Kimoto 1996, 1997; Marshall and Molteni 1993; Molteni 1996a,b). The same notion may be applied to the wind-driven ocean circulation. In particular, the low-frequency variability of the gyre circulation may be due to irregular transitions between multiple flow regimes. In this sense the analysis of multiple equilibria of the wind-driven circulation is directly connected with the low-frequency climate variability.

Ierley and Sheremet (1995) studied multiple equilibria of a barotropic single-gyre wind-driven model. Meacham and Berloff (1997) and Berloff and Meacham (1997) studied the low-dimensional attractors of the single-gyre model. The results of the single-gyre circulation are extended to the steady double-gyre wind forcing (Cessi and Ierley 1995; Speich et al. 1995; Jiang et al. 1995; Primeau 1998a,b; Scott and Straub 1998); these authors showed that, for a range of parameters, the circulation possesses multiple steady states. More precise-

---

*Corresponding author address:* Philip Sura, Meteorologisches Institut der Universität Hamburg, Bundesstraße 55, D-20146 Hamburg, Germany.  
E-mail: sura@dkrz.de

ly, these authors, except Jiang et al. (1995), explicitly computed fixed point solutions for a broad range of parameters. Jiang et al. use a time-dependent model to explore a parameter range where even a time-stepping procedure yields steady-state solutions. The quasigeostrophic double-gyre (Cessi and Ierley 1995; Primeau 1998a,b; Scott and Straub 1998) is characterized by two classes of steady states: One class consists of perfectly antisymmetric solutions and the other class consists of nonsymmetric solutions. The nonsymmetric solutions come in pairs due to the quasigeostrophic symmetry. Cessi and Ierley (1995) conjecture that all equilibria are of significance in the description of the low-frequency variability of the wind-driven circulation, regardless of their stability. Comparable experiments with the primitive equations were performed by Speich et al. (1995) and Jiang et al. (1995). Despite the fact that the primitive equations do not satisfy quasigeostrophic symmetry, they showed that the nonsymmetric equilibria come in pairs, in agreement with the quasigeostrophic calculations.

As usual in a forced dissipative system only one stable equilibrium exists if the wind forcing is very weak. As the forcing gets stronger, unstable modes appear successively leading finally to a chaotic behavior. More precisely, the stability transfer governed by the strength of the wind forcing, that is, the system nonlinearity, from stable stationary solutions to stable periodic solutions occurs through Hopf bifurcations. Further enhancement of the wind forcing causes the solution to pass from purely periodic to a more and more aperiodic behavior.

A rectangular basin with a zonal extension of  $L_x = 1000$  km and a meridional extension of  $L_y = 2000$  km is often used for the analysis of multiple equilibria in the case of the double-gyre wind forcing (Cessi and Ierley 1995; Speich et al. 1995; Jiang et al. 1995; Primeau 1998a; Scott and Straub 1998). Thus, a deeply penetrating jet is avoided by the basin geometry. However, a basin with a much larger zonal extension  $L_x$  reveals several deeply penetrating nonsymmetric and quasi-antisymmetric states (Primeau 1998b). The term “quasi-antisymmetric” is used to describe the flow structure where the mean transports of the northern and southern recirculation gyres are approximately equal. In the quasigeostrophic approximation the deeply penetrating quasi-antisymmetric circulation is the preferred regime reached by a time-stepping procedure, as long as a purely antisymmetric double-gyre wind forcing is used (McCalpin and Haidvogel 1996). Adding a mean wind-forcing asymmetry changes the qualitative structure of the circulation. The system appears to have several preferred regimes, as shown by McCalpin and Haidvogel (1996), which include a quasi-antisymmetric deeply penetrating state and a nonsymmetric weakly penetrating state. The latter state is caused by the asymmetry of the wind-forcing field. McCalpin and Haidvogel (1996) conclude that the low-frequency variability

of their model is due to irregular transitions between different regimes.

The present study uses a rectangular basin of 2400 km by 2400 km extent allowing a deeply penetrating jet. A double-gyre configuration is used to represent the mean wind field. The new aspect of this study is that the steady double-gyre forcing is made more realistic by adding a stochastic component, which is well known to play an important role in the excitation of oceanic low-frequency variability (Hasselmann 1976; Frankignoul and Hasselmann 1977; Frankignoul and Müller 1979; Frankignoul et al. 1997). The stochastic forcing mimics atmospheric weather fluctuations with spatially coherent white noise, whose variance is chosen to be spatially inhomogeneous. The spatially inhomogeneous variance of the stochastic forcing is introduced to parameterize the localized variability of the midlatitude atmospheric dynamics, whose intense synoptic-scale activity is related to storm tracks following the jet stream axes. Saravanan and McWilliams (1997) and Sura et al. (2000) show that the spatial inhomogeneity of the stochastic forcing could play an important part in producing low-frequency climate variability. The oceanic response to the known low-frequency meridional shift of the North Atlantic storm track due to the North Atlantic Oscillation (NAO) is not explored within this study.

McClintock (1999) stresses the importance of noise and its effects on physical systems and states that a proper appreciation of noise must involve studies of both the mechanisms that produce it, and the effect that it has on systems subject to it. A recent geophysical example about the effect of noise is given by Itoh and Kimoto (1996), who show that stochastic perturbations are able to force transitions among multiple atmospheric flow regimes. Therefore, the primary objective of this paper is to investigate the effect of the spatially inhomogeneous stochastic wind stress on the behavior of oceanic flow regimes.

In section 2 the reduced-gravity model, the wind stress forcing, and the corresponding numerical scheme are described. Section 3 presents the experimental design and the results of the numerical experiments. Finally, section 4 provides a discussion of the results.

## 2. Ocean model and atmospheric forcing

### a. Ocean model

The nonlinear reduced-gravity equations in transport form are used to model the upper ocean in a rectangular basin of 2400 km by 2400 km extent;  $(x, y)$  coordinates increasing eastward and northward are used. In the reduced-gravity approximation the ocean is represented by a single active layer of constant density  $\rho_1$  of thickness  $H$ . The upper-layer is assumed to overlie a deep and motionless layer of density  $\rho_2$ . With this constraint only the first baroclinic mode is modeled. That is, the interface between the two layers represents the per-

TABLE 1. Model parameters.

Coriolis parameter	$f = 1.03 \times 10^{-4} \text{ s}^{-1}$
Beta-effect	$\beta = 1.62 \times 10^{-11} \text{ m}^{-1} \text{ s}^{-1}$
Upper-layer equilibrium depth	$H_0 = 600 \text{ m}$
Rayleigh friction coefficient	$r = 1 \times 10^{-7} \text{ s}^{-1}$
Laplacian friction coefficient	$A = 2 \times 10^2 \text{ m}^2 \text{ s}^{-1}$
Upper-layer density	$\rho_1 = 1027 \text{ kg m}^{-3}$
Lower-layer density	$\rho_2 = 1030 \text{ kg m}^{-3}$
Reduced-gravity	$g' = 0.029 \text{ m s}^{-2}$
Wind stress amplitude	$\tau_0 = 0.05 \text{ N m}^{-2}$
Time step	$\Delta t = 1200 \text{ s}$
Domain extent (north–south)	$L_y = 2400 \text{ km}$
Domain extent (east–west)	$L_x = 2400 \text{ km}$
Grid resolution	$\Delta x = 20 \text{ km}$ $\Delta y = 20 \text{ km}$

manent thermocline. The eastward and northward transport is defined as  $U = uH$  and  $V = vH$ , whereby  $u$  and  $v$  are the corresponding velocities,  $\tau^x$  and  $\tau^y$  are the wind stress components,  $g$  is the acceleration of gravity, and  $f$  is the Coriolis parameter given by the  $\beta$ -plane approximation,  $f = f_0 + \beta y$ . Thus, the equations are

$$\begin{aligned} \frac{\partial U}{\partial t} + \frac{\partial}{\partial x} \left( \frac{U^2}{H} \right) + \frac{\partial}{\partial y} \left( \frac{UV}{H} \right) - fV \\ = \frac{-g'}{2} \frac{\partial H^2}{\partial x} + \frac{\tau^x}{\rho_1} - rU + A\Delta U \end{aligned} \quad (1)$$

$$\begin{aligned} \frac{\partial V}{\partial t} + \frac{\partial}{\partial x} \left( \frac{UV}{H} \right) + \frac{\partial}{\partial y} \left( \frac{V^2}{H} \right) + fU \\ = \frac{-g'}{2} \frac{\partial H^2}{\partial y} + \frac{\tau^y}{\rho_1} - rV + A\Delta V \end{aligned} \quad (2)$$

$$\frac{\partial H}{\partial t} + \frac{\partial U}{\partial x} + \frac{\partial V}{\partial y} = 0, \quad (3)$$

where the reduced-gravity is  $g' = g(\rho_2 - \rho_1)/\rho_2$ .

Interfacial friction is parameterized by Rayleigh friction scaled by  $r$ ; the lateral viscosity is represented by a Laplacian scaled by  $A$ . All parameters of the model are summarized in Table 1. For dynamical parameters standard numerical values are used. The Laplacian friction coefficient is chosen to adjust the width of the dimensional Munk layer  $\delta_M^* = (A/\beta)^{1/3}$  to approximately the width of the numerical grid.

The dynamics of the wind-driven model is controlled by several nondimensional parameters. The parameters, derived from the nondimensional form of the barotropic quasigeostrophic vorticity equation (e.g., Pedlosky 1996), are the dimensional inertial, Stommel, and Munk layer thickness scaled by the width of the basin (the asterisk denotes dimensional values)

$$\begin{aligned} \delta_I = \frac{\delta_I^*}{L_x} = \left( \frac{U}{\beta L_x^2} \right)^{1/2}, \quad \delta_S = \frac{\delta_S^*}{L_x} = \frac{r}{\beta L_x}, \\ \delta_M = \frac{\delta_M^*}{L_x} = \left( \frac{A}{\beta L_x^3} \right)^{1/3}. \end{aligned} \quad (4)$$

The velocity scale in the interior,  $U$ , and a characteristic value of the wind stress,  $\tau$ , are connected by the Sverdrup relation. For a rectangular basin with a double-gyre wind stress the scaling reads  $U = (2\pi\tau)/(\rho_1\beta L_y H_0)$  (then  $\tau$  is the amplitude of the double-gyre forcing). The three parameters measure the importance of the nonlinearity, bottom friction, and lateral diffusion. In particular, the relative importance of the nonlinearity and the lateral diffusion is often expressed through the boundary layer Reynolds number

$$\text{Re} = \left( \frac{\delta_I}{\delta_M} \right)^3. \quad (5)$$

For the parameters used in the present study (Table 1) the dimensional Stommel and Munk layer widths are  $\delta_S^* = 6.17 \text{ km}$  and  $\delta_M^* = 23.11 \text{ km}$  (nondimensional values:  $\delta_S = 2.571 \times 10^{-3}$ ,  $\delta_M = 9.629 \times 10^{-3}$ ). For a typical wind stress value of  $0.05 \text{ N m}^{-2}$  the dimensional inertial layer width is  $\delta_I^* = 28.44 \text{ km}$  (nondimensional value:  $\delta_I = 1.185 \times 10^{-2}$ ). This gives a boundary layer Reynolds number of  $\text{Re} = 1.86$ .

The equations of motion are solved numerically on a staggered Arakawa C grid. The model resolution is 20 km in both the zonal and meridional direction. Time differencing is performed by the Matsuno (Euler backward) scheme, space differencing by space-centered finite difference approximations. The nonlinear advection terms are computed by first averaging the prognostic variables in space to calculate the required products at the appropriate mesh points before the centered finite differences are calculated. The no-flux boundary condition is used to suppress the normal flow at the boundaries. Furthermore, the tangential boundary condition is a linear combination of tangential velocity and stress

$$\gamma \mathbf{u} \cdot \mathbf{t} + (1 - \gamma) \mathbf{n} \cdot \nabla(\mathbf{u} \cdot \mathbf{t})|_C = 0, \quad (6)$$

where  $\mathbf{t}$  is the unit vector tangent to the domain boundary  $C$  and  $\mathbf{n}$  is the unit vector normal to  $C$ . The parameter  $\gamma$  has the limiting values for no-slip ( $\gamma = 1$ ) and free-slip ( $\gamma = 0$ ) boundary conditions. For this reason, (6) is normally designated as a partial-slip boundary condition. For the major part of this study (section 3a) a half-slip condition ( $\gamma = 0.5$ ) is employed. The choice of the half-slip condition is due to Haidvogel et al. (1992), who suggest that the tangential velocities at the boundaries should lie between the no-slip and the free-slip limits. The sensitivity of the presented results to changes of the boundary conditions, that is, other values of  $\gamma$ , is discussed in section 3c. In addition, the sensitivity to changes of the initial conditions and the basin size are discussed in same section.

Two standard definitions are introduced that are used throughout the remainder of the paper. The layer thickness  $H$  is the sum of the equilibrium depth  $H_0$  and the depth anomaly  $h$  so that  $H(x, y, t) = H_0 + h(x, y, t)$ . Furthermore, all time-dependent variables, for example,  $\psi$ , are divided into a long term mean  $\bar{\psi}$  and a deviation  $\psi'$  such that  $\psi = \bar{\psi} + \psi'$ .

### b. Atmospheric forcing

The atmospheric forcing of the ocean by the wind stress consists of a mean field and a stochastic field

$$\boldsymbol{\tau} = \boldsymbol{\tau}_{\text{mean}} + \boldsymbol{\tau}_{\text{stochastic}}. \quad (7)$$

The mean wind stress  $\boldsymbol{\tau}_{\text{mean}}$  is represented by a zonal wind field with a sinusoidal pattern

$$\tau_{\text{mean}}^x = \phi \tau_0 \cos\left(\frac{2\pi y}{L_y}\right), \quad -\frac{L_y}{2} \leq y \leq \frac{L_y}{2}. \quad (8)$$

This generates a northern cyclonic subpolar and a southern anticyclonic subtropical gyre. The reference wind stress amplitude  $\tau_0$  is set to a standard value of  $0.05 \text{ N m}^{-2}$ . Recognize that the amplitude of the fluid motion and hence the nonlinearity of the system is proportional to the strength of the wind stress. Therefore, nonlinear effects can be studied by varying the wind stress parameter  $\phi$ . The value of  $\phi$  is chosen to range between 0.7 and 1.3. Because the boundary layer Reynolds number for the reference wind stress amplitude  $\tau_0$  is  $\text{Re} = 1.86$ , the value of  $\text{Re}$  for different wind stress parameters is  $\text{Re} = 1.86\phi^{3/2}$ . Thus,  $\text{Re}$  has values between 1.09 and 2.76.

The spatially inhomogeneous stochastic forcing  $\boldsymbol{\tau}_{\text{stochastic}}$  accounts for the high-frequency atmospheric variability and is parameterized by the bulk formula for the wind stress. The bulk formula is preferred to the direct use of the wind stress components as it renders possible to preserve the eddy kinetic energy of the atmosphere in all experiments. This leads to the parameterization of the spatially inhomogeneous stochastic forcing

$$\begin{aligned} \boldsymbol{\tau}_{\text{stochastic}} &= \rho_{\text{air}} C_D |\mathbf{u}'| \mathbf{u}', \\ u'(x, y, t) &= \eta_x(t) f(x, y), \\ v'(x, y, t) &= \eta_y(t) f(x, y), \end{aligned} \quad (9)$$

where  $\rho_{\text{air}}$ ,  $|\mathbf{u}'|$ , and  $\mathbf{u}'$  are the air density ( $1.3 \text{ kg m}^{-3}$ ), near-surface wind speed, and velocity;  $C_D$  ( $2 \times 10^{-3}$ ) is the drag coefficient; and  $\eta_{x,y}(t)$  are independent white noise processes with zero mean and standard deviation  $\sigma$ . In the numerical integration the white noise is updated once a day. The weight function  $f(x, y)$  parameterizes the spatial structure of the atmospheric variability by a Gaussian shape, whose origin is placed in the center of the basin

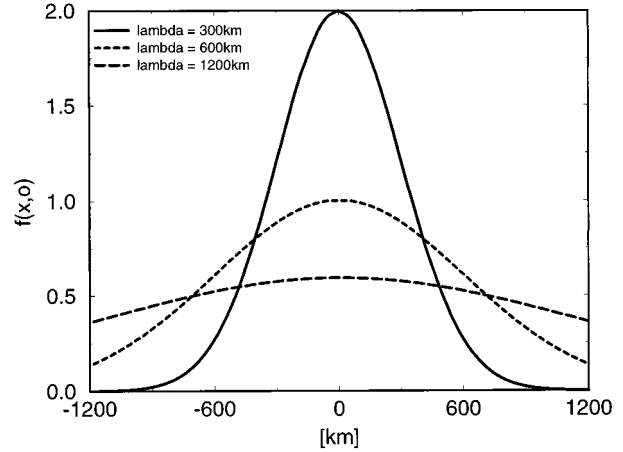


FIG. 1. The shape of the weight function  $f(x, y)$  for different values of the inhomogeneity parameter  $\lambda$  at  $y = 0$ . The choice of the scaling constant  $\alpha$  is described in the text.

$$\begin{aligned} f(x, y) &= \frac{\alpha}{\left[ \pi \lambda_x \lambda_y \operatorname{erf}\left(\frac{L_x}{2\lambda_x}\right) \operatorname{erf}\left(\frac{L_y}{2\lambda_y}\right) \right]^{1/2}} \\ &\quad \times \exp\left(-\frac{x^2}{2\lambda_x^2} - \frac{y^2}{2\lambda_y^2}\right) \end{aligned} \quad (10)$$

with the error function  $\operatorname{erf}$ . The denominator normalizes the area integral of the squared weight function over the basin domain  $\Omega$  to unity, and  $\alpha$  is a scaling constant. The inhomogeneity parameters,  $\lambda_x$  and  $\lambda_y$ , control the spatial structure of the atmospheric variability. To obtain circular symmetry of the stochastic forcing,  $\lambda_x = \lambda_y = \lambda$ . The Gaussian shape with circular symmetry is chosen for convenience to parameterize the localized atmospheric eddy activity along the storm tracks in a conceptual manner. The physical motivation for the particular weight function is that the observed climatological position of the North Atlantic storm track maximum is approximately coincident with that of the observed mean zero wind stress curl line. The low-frequency meridional shift of the storm track due to NAO is not included in the used parameterization.

The shapes associated with different  $\lambda$  values used in the subsequent numerical experiments are shown in Fig. 1. The scaling constant  $\alpha$  is chosen to adjust the weight function in the origin to 1 for  $\lambda = 600 \text{ km}$ . Thus  $\alpha = [\pi \lambda_x \lambda_y \operatorname{erf}(L_x/2\lambda_x) \operatorname{erf}(L_y/2\lambda_y)]^{1/2}$  with  $\lambda_x = \lambda_y = 600 \text{ km}$ . The variance  $\sigma^2$  of the white noise is  $28 \text{ m}^2 \text{ s}^{-2}$ , characterizing the observed atmospheric conditions in the North Atlantic region. That is, the variance of the wind speed in the center of the basin is comparable to the observed conditions (Wright 1988). Nevertheless, the stochastic forcing has to be understood as a conceptual tool to study the effect of noise on simple wind-driven ocean models.

### 3. Numerical experiments: Design and results

The experimental design focuses on the nonlinear behavior of the wind-driven double-gyre circulation in the presence of a spatially inhomogeneous stochastic forcing. For this reason, the parameters varied are the strength of the mean wind stress ( $\phi$ ) and the inhomogeneity of the stochastic forcing ( $\lambda$ ). All other parameters remain unchanged. In particular, a half-slip boundary condition ( $\gamma = 0.5$ ) is used for the basic experiments described in sections 3a,b. For every value of  $\phi$ , varying between 0.7 and 1.3, the effect of the stochastic wind stress is analyzed by four different experiments. Three experiments are defined by the inhomogeneity parameters  $\lambda = 300, 600,$  and  $1200$  km. In addition, a corresponding run without stochastic forcing is performed. All experiments described in sections 3a,b commence from a resting state; the sensitivity to changes of the initial conditions is discussed in section 3c. The experiments including the stochastic forcing are integrated for 510 years. The experiments without stochastic forcing are integrated for at least 110 years; the actual duration depends on the specific behavior of the experiment. The first 10 years are always skipped to account for the spinup phase. Transports, velocities, and depth anomalies are saved once a day. For all further diagnostics monthly means are used to calculate the basin integrated eddy energies (see below) because it is reasonable to employ the period of the nondispersive first baroclinic Rossby mode in midlatitudes as an appropriate timescale, which has the order of years. Annual means are used to present snapshots of the time-dependent flow patterns.

A convenient overall description of the transient behavior of the basin circulation can be given in terms of the integrated eddy energy content in the basin domain  $\Omega$ . The basin-integrated eddy kinetic and eddy potential energies are defined by

$$[E'_{\text{kin}}]_{\Omega} = \frac{1}{\Omega} \int \int_{\Omega} \left( \frac{\rho_1 \bar{H}}{2} (u'^2 + v'^2) \right) dx dy \quad (11)$$

$$[E'_{\text{pot}}]_{\Omega} = \frac{1}{\Omega} \int \int_{\Omega} \left( \frac{g' \rho_1 h'^2}{2} \right) dx dy. \quad (12)$$

The brackets with the  $\Omega$  subscript denote the basin average. Furthermore, the volume transport streamfunction  $\psi$  is used to show the structure of the flow patterns:  $U = -\partial\psi/\partial y$ ,  $V = \partial\psi/\partial x$ . This is done to lay emphasis on the symmetry properties of the double-gyre solutions. In the subsequent discussion the term ‘‘quasi-stable’’ is used to characterize that the circulation does not change its overall flow structure in time.

#### a. The reference case: $\phi = 1$

The set of experiments with  $\phi = 1$  is chosen to be the reference case described first. This reference case

shows the main results of the present paper and, therefore, is analyzed in greater detail. The discussion of the sensitivity to a varying wind stress parameter  $\phi$  follows in section 3b.

The time series of the basin-integrated eddy energies of the four experiments are shown in Fig. 2. For clarity, only the first 200 years of the experiments with the stochastic forcing are presented. The remaining 300 years are visually similar. For the corresponding experiment without stochastic forcing 100 years are shown in Fig. 2.

The experiment without the stochastic forcing exhibits a purely periodic oscillation with a period of about 3 yr. The corresponding time-averaged flow pattern (Fig. 3) shows the classical quasi-antisymmetric double-gyre pattern with a free jet of about 1000-km penetration scale; a weak meander occurs about 600 km downstream. Animation of the flow field reveals that this pattern is quasi-stable; only the eastward extreme of the jet shows a weak oscillation, which, however, does not change the overall flow regime (not shown). It is well known that the double-gyre model possesses (even multiple) periodic solutions for a moderate range of Reynolds numbers. This phenomenon is well documented for different basin dimensions (Speich et al. 1995; Jiang et al. 1995; Dijkstra and Katsman 1997). The solutions pass from purely periodic oscillations to a more and more aperiodic behavior for increasing zonal basin extensions at fixed forcing and dissipative parameters.

Adding the spatially nearly homogeneous stochastic forcing to the mean double-gyre wind stress ( $\lambda = 1200$  km), the behavior of the eddy energy time series changes. The variance of the transient motion increases and the periodicity is destroyed by the stochastic forcing. Nevertheless, the large-scale flow pattern does not change its quasi-antisymmetric structure and is, therefore, qualitatively similar to the experiment without stochastic forcing. The persistence of the quasi-antisymmetric flow is shown by snapshots of representative circulation patterns (Fig. 4).

Decreasing the inhomogeneity parameter  $\lambda$  to 600 km enhances the overall eddy energy level and the variance because the wind stress curl of the stochastic forcing driving the large-scale ocean circulation increases with decreasing  $\lambda$ . Periods with relative high eddy energies appear. The high eddy energy phases are characterized by a slightly stronger meandering jet in combination with a reduced penetration scale of about 800 km. The low energy phases show the quasi-antisymmetric structure as described before. The large-scale structure of the zonally penetrating free jet, however, is preserved throughout the high and low eddy energy periods.

Further enhancement of the spatial inhomogeneity ( $\lambda = 300$  km) gives rise to a flow regime that is not observed in the previous experiments. An examination of the flow patterns reveals a highly nonsymmetric regime, which the flow attains temporarily. This nonsymmetric regime is adopted twice in the first 200 years of the

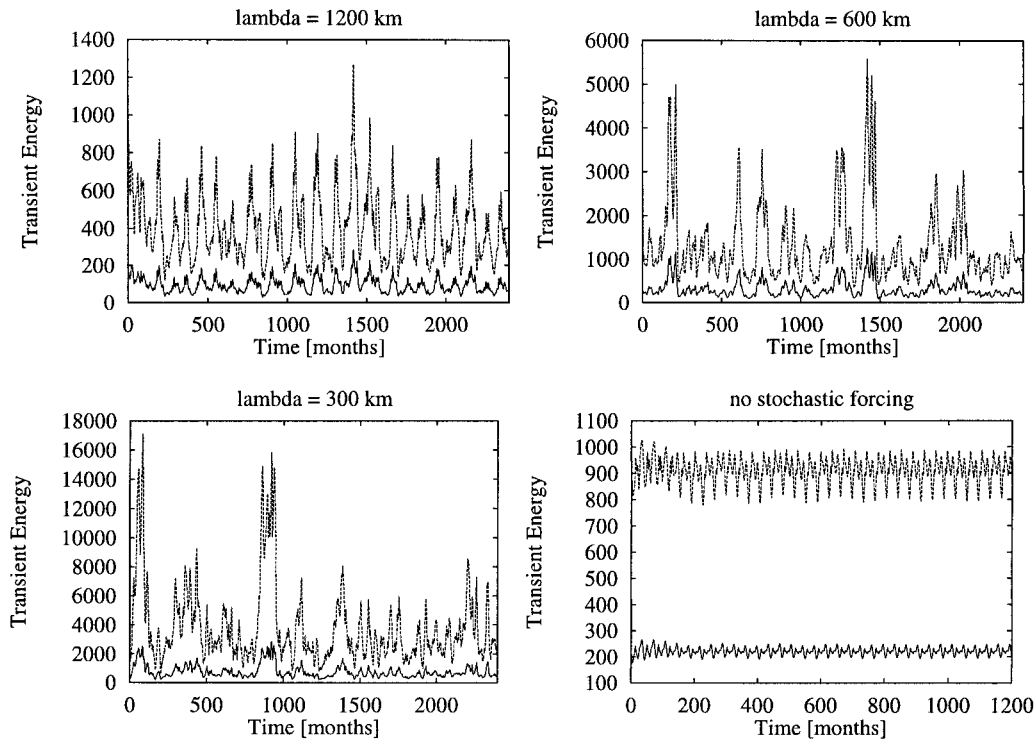


FIG. 2. Time series of basin-integrated eddy energies ( $\text{J m}^{-2}$ ) for  $\phi = 1$ . The dashed lines denote the eddy potential energies, the solid lines the eddy kinetic energies. Note the different time range for the experiment without stochastic forcing.

integration. It is associated by very high eddy energies (near months 100 and 750; see Fig. 2) and persists for approximately 10 years before returning to the low eddy energy state. The quasi-antisymmetric low eddy energy phases are comparable to the experiment with  $\lambda = 600$

km. Thus, in the experiment with  $\lambda = 300$  km the circulation exhibits a bimodal behavior between a quasi-antisymmetric and a nonsymmetric state. Figure 5 presents the low eddy energy state as a quasi-antisymmetric circulation, whereas the high eddy energy state shows a nonsymmetric circulation pattern characterized by a northward displacement of the jet in connection with an enhanced transport in the cyclonic northern recirculation gyre. It seems that the nonsymmetric regime corresponds to one member of a known nonsymmetric pair of stationary solutions that is found in larger basins with a zonal extension of  $L_x = 3600$  km and a meridional extension of  $L_y = 2800$  km (Primeau 1998a). The other member of the pair, characterized by a southward displacement of the jet in connection with an enhanced transport in the anticyclonic recirculation gyre, does not appear. The regime transition from the quasi-antisymmetric low eddy energy state to the nonsymmetric high eddy energy state is shown by snapshots of representative circulation patterns (Fig. 6). The transition is initiated by an abnormal positive curvature of the entire jet (year 1). One year later (year 2) the eastward extension of the jet moved northward and shows now an anticyclonic recirculation cell in addition to the recirculation pattern near the western boundary. Finally, year 3 shows the nonsymmetric flow regime persisting for about 10 years. The high eddy activity is due to a pulsating behavior of the recirculation gyres that is com-

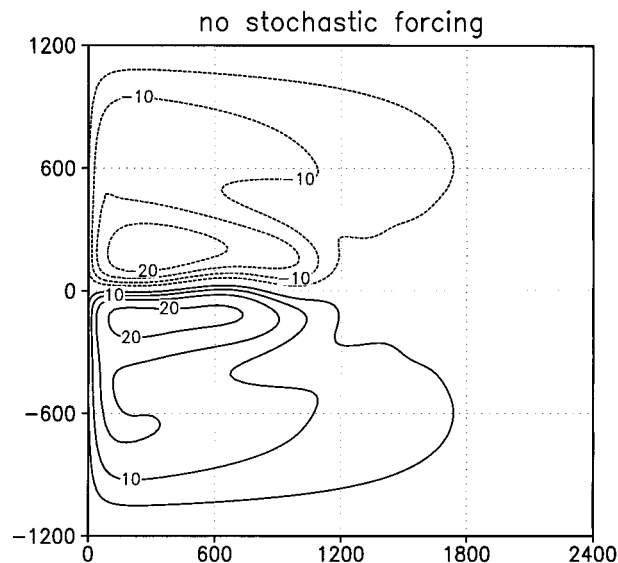


FIG. 3. Time-averaged volume transport streamfunction ( $10^6 \text{ m}^3 \text{ s}^{-1}$ ) for  $\phi = 1$ ; no stochastic forcing. The axes are horizontal distances in kilometers.

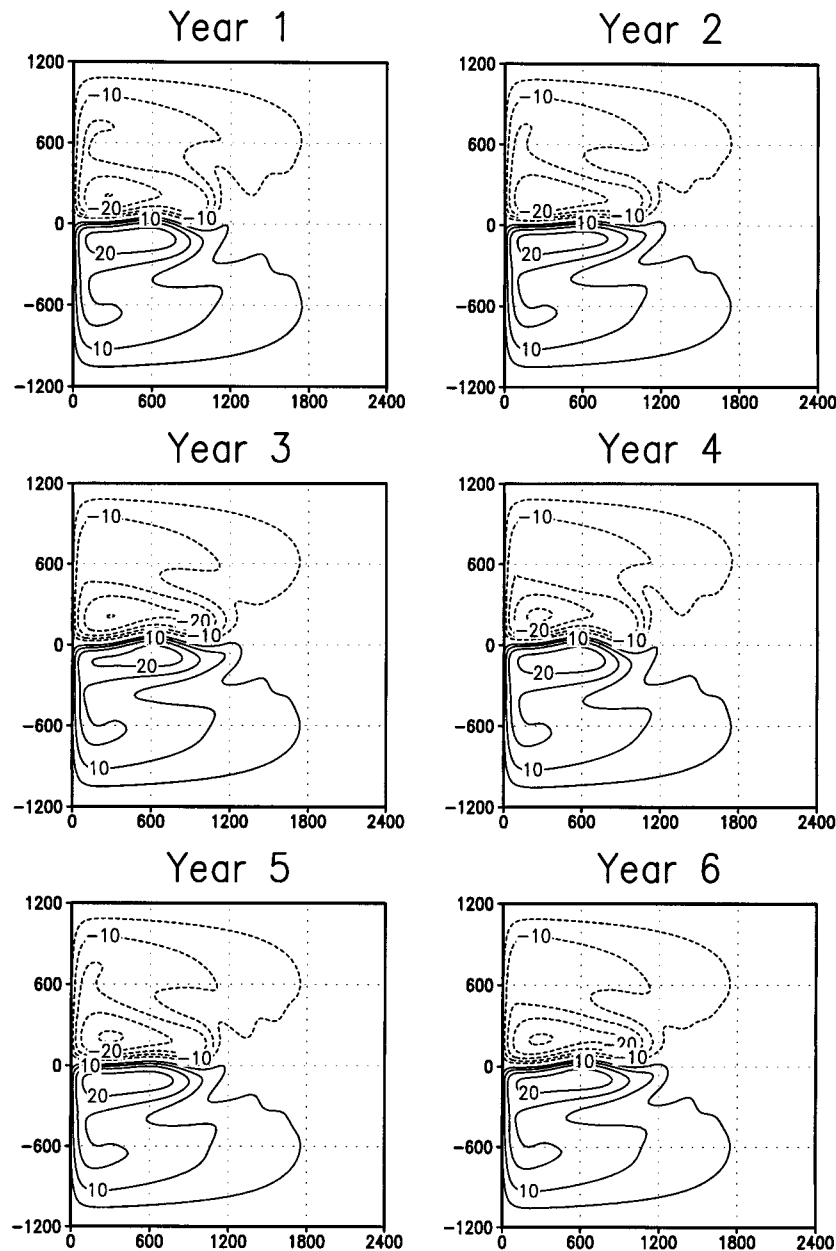


FIG. 4. Snapshots of representative volume transport streamfunction fields ( $10^6 \text{ m}^3 \text{ s}^{-1}$ ) for  $\phi = 1$  and  $\lambda = 1200 \text{ km}$ . The axes are horizontal distances in kilometers.

parable to the periodic and aperiodic behavior, that, in the case of no stochastic forcing, has been described by Jiang et al. (1995), Speich et al. (1995), and Dijkstra and Katsman (1997). The pulsating behavior is not clearly seen in the annually averaged fields (Fig. 6) because it has a typical timescale of several months. The corresponding anomalies (Fig. 7) reveal that the positive curvature of the jet that initiates the regime transition is caused by a strong negative anomaly near the western boundary (year 1). The anticyclonic recirculation cell appears one year later at the eastward end

of the jet, which is due to a positive anomaly moving farther west in the following years. The regime transition back into the quasi-antisymmetric, low eddy energy state is shown by the streamfunction snapshots (Fig. 8). In year 10, the northern extension of the recirculation gyre has moved westward and begins to detach. One year later (year 11) the detachment process has finished and the detached eddy can still be seen near the western boundary within the subpolar gyre. In the following years the free jet penetrates into the basin, finally giving rise to the quasi-antisymmetric circulation pattern again.

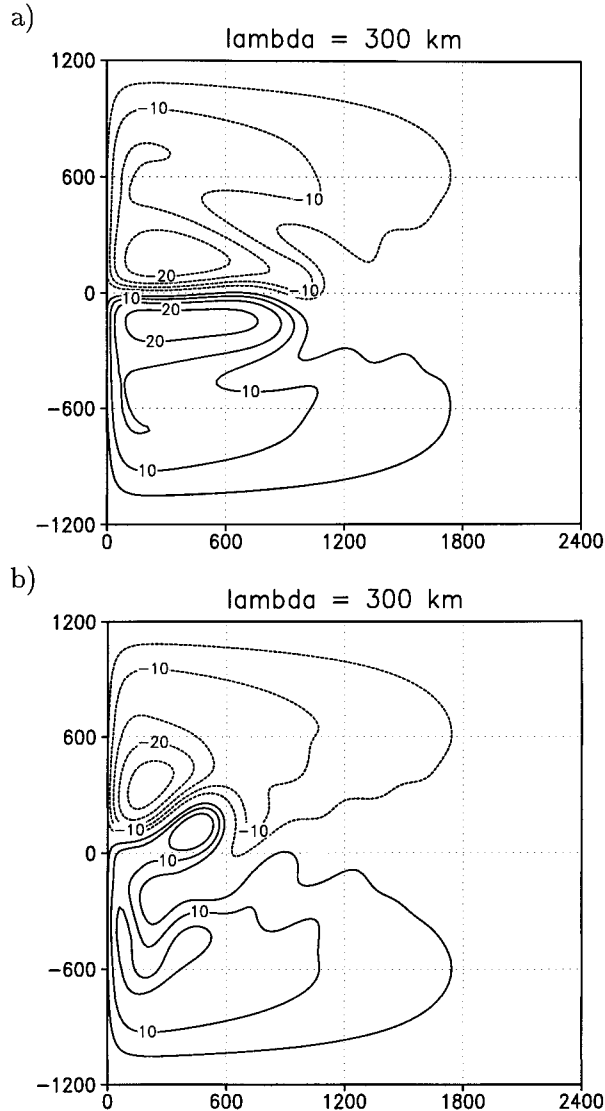


FIG. 5. Representative volume transport streamfunction fields ( $10^6 \text{ m}^3 \text{ s}^{-1}$ ) for the two different regimes in the experiment with  $\phi = 1$  and  $\lambda = 300 \text{ km}$ : (a) represents the low eddy energy state and (b) the high eddy energy state. The axes are horizontal distances in kilometers.

### b. Sensitivity to the wind stress parameter $\phi$

The time series of the basin-integrated eddy energies of the experiments with  $\phi = 1.1, 1.2,$  and  $1.3$  are shown in Fig. 9. For convenience, only the time series for the experiments of intermediate ( $\lambda = 600 \text{ km}$ ) and maximum stochastic forcing inhomogeneity ( $\lambda = 300 \text{ km}$ ) are shown; they generate regime transitions. As before, only the first 200 years of the experiments with the stochastic forcing are presented. The remaining years are visually similar.

With  $\phi = 1.1$  the experiment without stochastic forcing exhibits a nearly periodic oscillation. The familiar change in the phenomenology of the time series is the

increase of the eddy energy as the wind stress magnitude is increased. Nevertheless, the large-scale flow still shows the quasi-antisymmetric double-gyre pattern with a free jet whose penetration scale is slightly increased in comparison to the corresponding reference experiment with  $\phi = 1$ . The almost homogeneous stochastic forcing ( $\lambda = 1200 \text{ km}$ ) enhances the variability, but does not change the quasi-antisymmetric structure of the flow. Increasing the inhomogeneity ( $\lambda = 600 \text{ km}$ ) the behavior of the flow changes as compared to the corresponding reference experiment. The regime transition occurs even for the intermediate inhomogeneity. This is seen by the time series peaks near months 1500 and 1800 in Fig. 9. The phenomenology of the antisymmetric and the nonsymmetric regime and the regime transition is the same as for the reference case. Thus, the streamfunction fields of the two regimes shown in Fig. 5 and the snapshots of the regime transition presented in Figs. 6, 7, and 8 are representative for the bimodal behavior even for the experiment with an intermediate inhomogeneity and  $\phi = 1.1$ . Further enhancement of the inhomogeneity of the stochastic forcing ( $\lambda = 300 \text{ km}$ ) does not lead to significant changes as compared to the corresponding reference experiment; the clear regime transitions are still present in the case of an increased amplitude of the double-gyre wind forcing. As before, the regimes and the regime transitions are equal to the described reference case.

For  $\phi = 1.2$  the experiment without stochastic forcing still runs into a periodic oscillation. Nevertheless, it takes a long time until the flow settles down in the periodic solution. This behavior is a manifestation of the increased nonlinearity of the system. As in the previously discussed experiments the circulation shows the familiar quasi-antisymmetric structure. The same holds for the experiment with the nearly homogeneous stochastic forcing ( $\lambda = 1200 \text{ km}$ ) with the restriction that the jet begins to show stronger transient meandering. Thus, the jet is easily destabilized by the stochastic forcing without showing regime transitions. In the experiment with an intermediate inhomogeneity ( $\lambda = 600 \text{ km}$ ) one extreme event occurs during the first 200 years of the integration. Further increase of the inhomogeneity of the stochastic forcing to  $\lambda = 300 \text{ km}$  makes a clear identification of the regimes rather difficult. Animation of the flow reveals that the nonsymmetric regime is still adopted, but with very short residence durations.

For  $\phi = 1.3$  the experiment without stochastic forcing behaves aperiodically, still showing the quasi-antisymmetric structure with enhanced transports. Again the same holds for the experiment with the nearly homogeneous stochastic forcing ( $\lambda = 1200 \text{ km}$ ). The experiment with an intermediate inhomogeneity ( $\lambda = 600 \text{ km}$ ) does not show regime transition for  $\phi = 1.3$ . It is interesting to recognize that a further increase of the inhomogeneity of the stochastic forcing to  $\lambda = 300 \text{ km}$  leads to very clear regime transitions in contrast to the comparable experiment with  $\phi = 1.2$ . Even the resi-

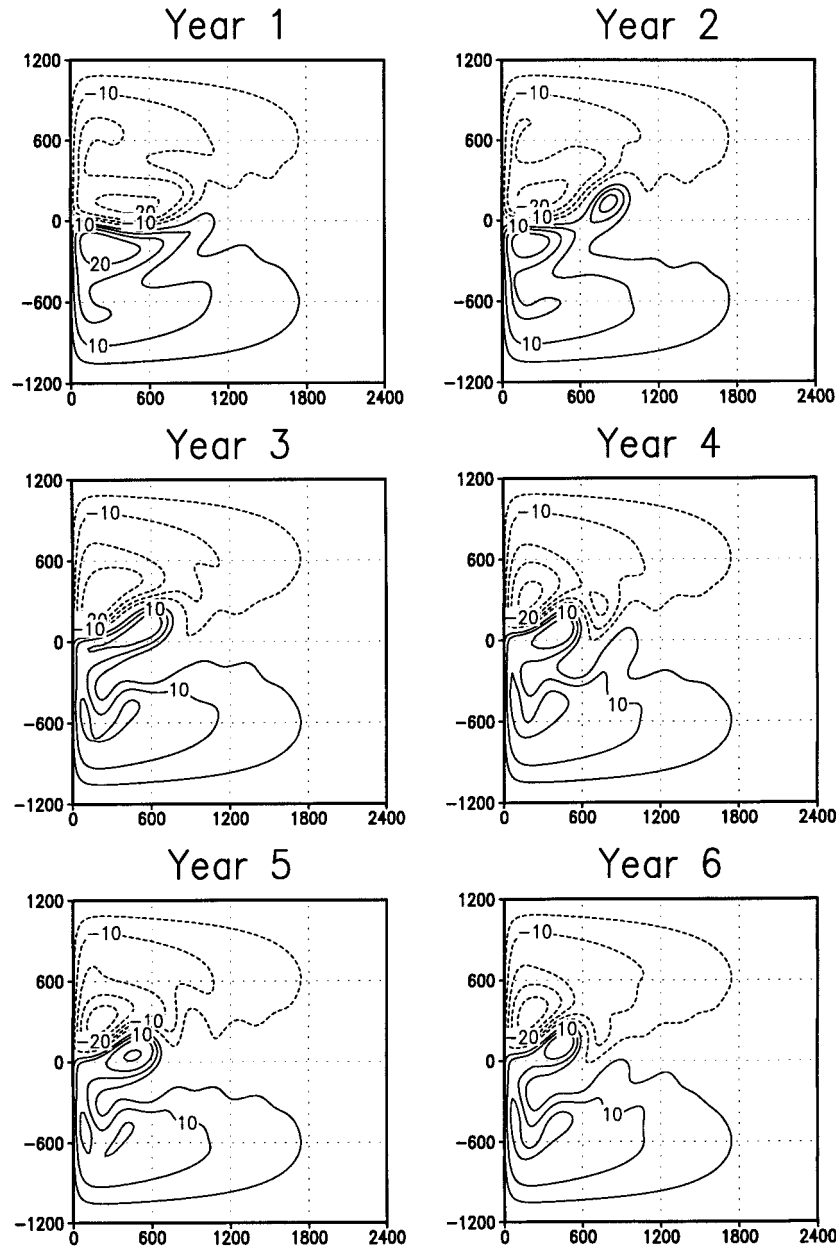


FIG. 6. Snapshots of representative volume transport streamfunction fields ( $10^6 \text{ m}^3 \text{ s}^{-1}$ ) for  $\phi = 1$  and  $\lambda = 300 \text{ km}$ . Note the regime transition. The axes are horizontal distances in kilometers.

dence time of the nonsymmetric regime becomes very long; the system remains in that regime for 20–50 yr. Thus, the change in the behavior of the system with increasing wind stress magnitude is quite subtle.

For wind stress parameters  $\phi = 0.9, 0.8,$  and  $0.7$  the experiments without stochastic forcing can be summarized by the fact that they all show a periodic behavior. Decreasing the wind stress amplitude decreases the penetration scale of the free jet in connection with a decreased amplitude of the oscillation. Furthermore, the system remains in the quasi-antisymmetric regime.

Likewise, the experiments with stochastic forcing exhibit a somehow simpler behavior than the experiments with higher values of  $\phi$ . Indeed, the experiments with the intermediate ( $\lambda = 600 \text{ km}$ ) and the maximum ( $\lambda = 300 \text{ km}$ ) inhomogeneity show a clearly weakened bimodal behavior. As before, the experiments with a nearly homogeneous stochastic forcing ( $\lambda = 1200 \text{ km}$ ) do not show regime transitions.

With  $\phi = 0.9$  the intermediate inhomogeneity experiment with  $\lambda = 600 \text{ km}$  does not exhibit regime transitions; only the quasi-antisymmetric regime is pre-

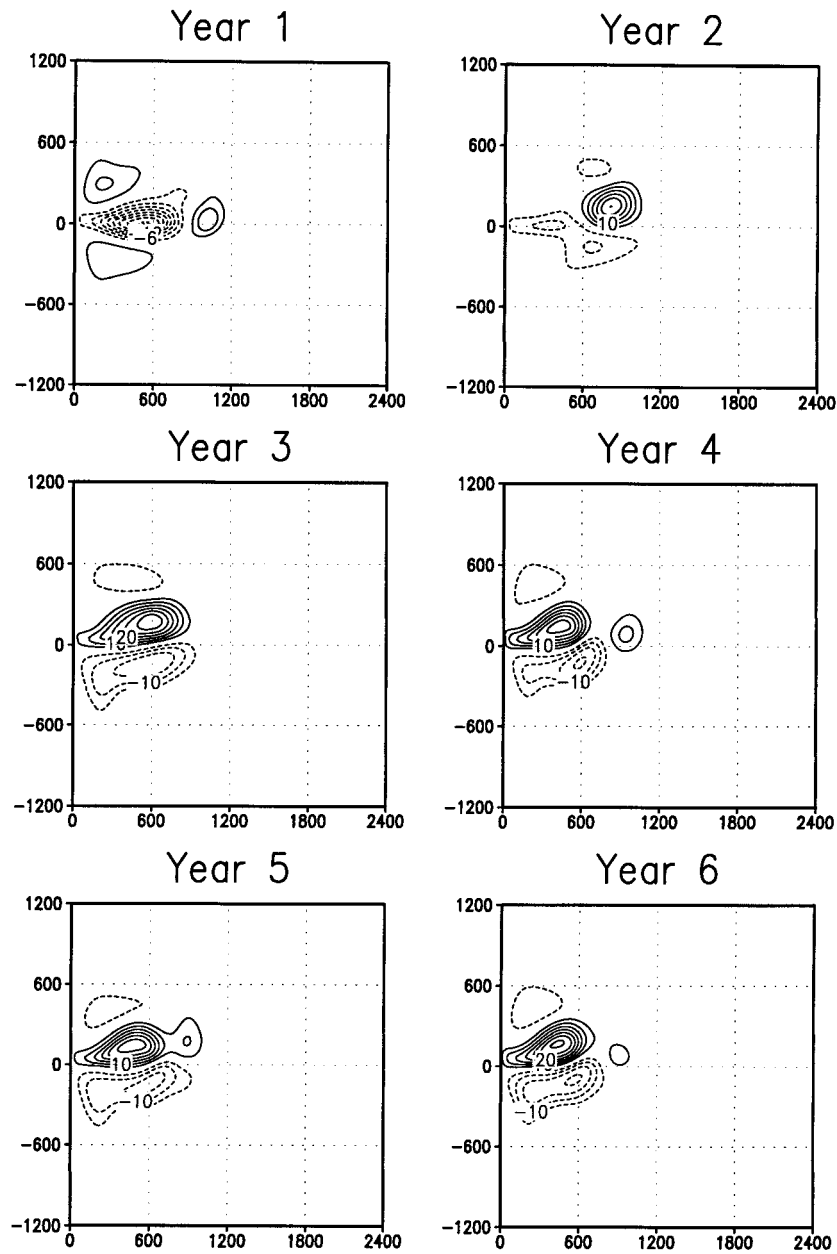


FIG. 7. Snapshots of representative volume transport streamfunction anomalies ( $10^6 \text{ m}^3 \text{ s}^{-1}$ ) for  $\phi = 1$  and  $\lambda = 300 \text{ km}$ . Note the regime transition. The axes are horizontal distances in kilometers.

sent in this case. Nevertheless, the experiment with the maximum inhomogeneity ( $\lambda = 300 \text{ km}$ ) does show transitions between the regimes. Their persistence of about one year, however, is very short. The regime transitions occur as described previously for the reference experiment with  $\phi = 1$ . But, immediately after the nonsymmetric regime is established, the detachment process of the recirculation gyre begins. Thus, the nonsymmetric regime is not persistent any more. The remaining sets of experiments with  $\phi = 0.8$  and  $0.7$  do not show regime transitions at all.

*c. Sensitivity to boundary conditions, initial conditions, and basin size*

1) BOUNDARY CONDITIONS

It is well known that the solutions of the wind-driven ocean circulation depend sensitively on boundary conditions that are poorly known from observations. Therefore, it is important to know how the solutions are affected by different boundary conditions. Detailed sensitivity experiments that span the no-slip and free-slip limits are reported by Haidvogel et al. (1992) using a

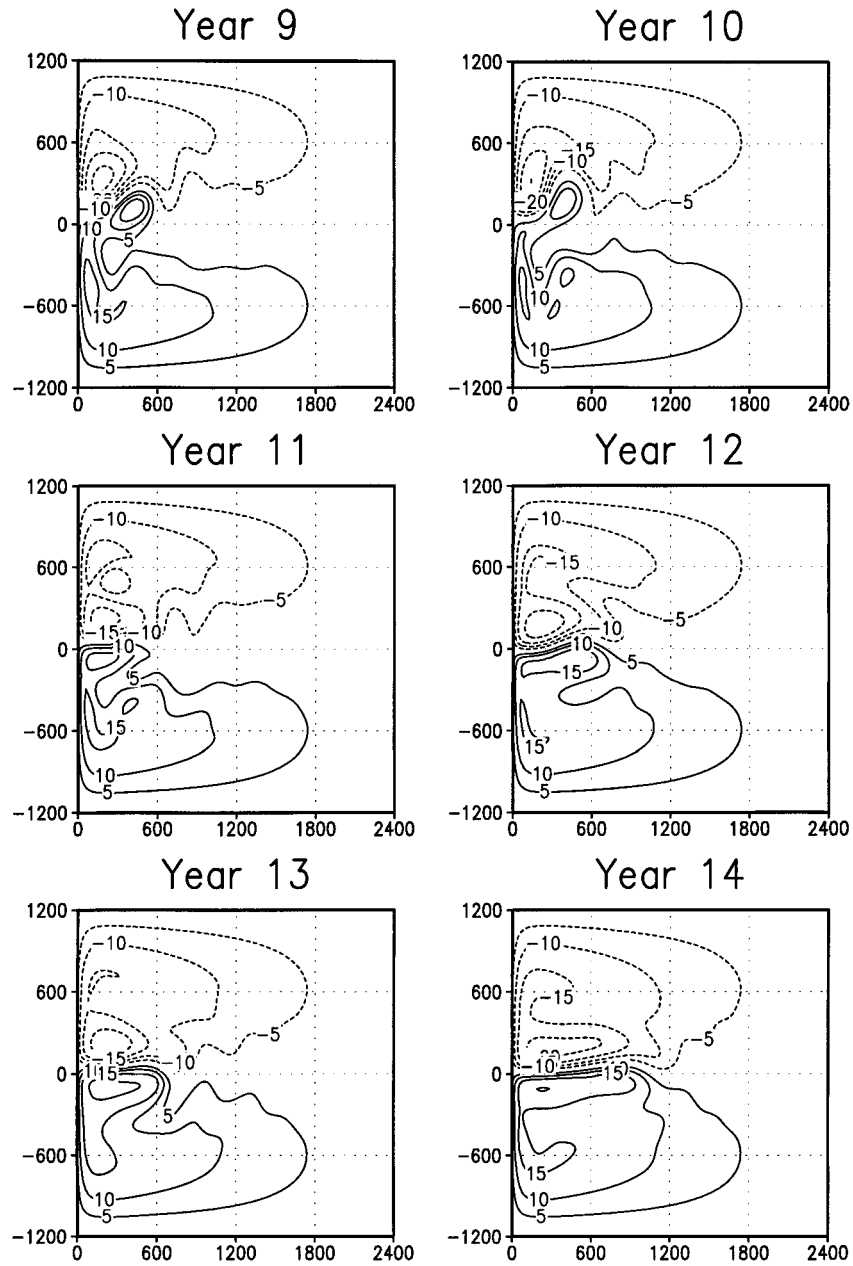


FIG. 8. Snapshots of representative volume transport streamfunction fields ( $10^6 \text{ m}^3 \text{ s}^{-1}$ ) for  $\phi = 1$  and  $\lambda = 300 \text{ km}$ . Note the regime transition. The axes are horizontal distances in kilometers.

basin with a large zonal extension of  $L_x = 3600 \text{ km}$ . In general, with increasing  $\gamma$  the model becomes more energetic and the jet penetrates farther into the basin. In the present study, the no-slip ( $\gamma = 1$ ) and the free-slip ( $\gamma = 0$ ) limits are explored within this section. The experimental setup is the same as in the previous section. Thus, the strength of the mean wind stress ( $\phi$ ) and the inhomogeneity of the stochastic forcing ( $\lambda$ ) are varied. As before, a corresponding run without stochastic forcing is performed.

The use of no-slip ( $\gamma = 1$ ) and free-slip ( $\gamma = 0$ ) conditions do not change the general results of the previous section. Indeed, for no-slip and free-slip boundaries the large-scale circulation structure of the experiments without stochastic forcing shows a quasi-antisymmetric flow pattern. With the same mean wind stress forcing, no-slip boundaries make the flow more stable. The occurrence of the stochastically induced regime transitions is shifted to somewhat larger wind stress parameters  $\phi$ , that is, to a slightly more nonlinear region

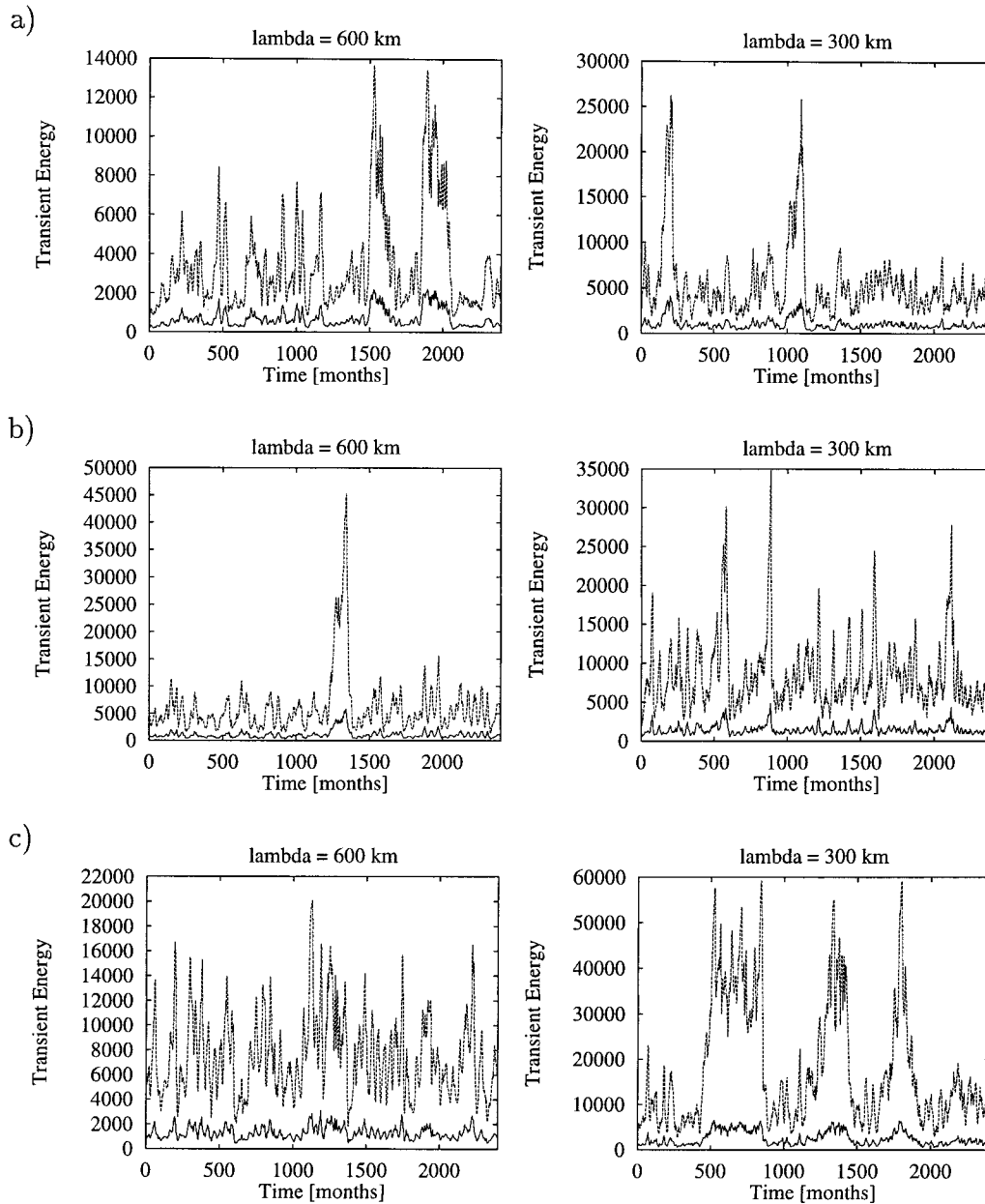


FIG. 9. Time series of basin-integrated eddy energies ( $\text{J m}^{-2}$ ) for different values  $\phi$ . The dashed lines denote the eddy potential energies, the solid lines the eddy kinetic energies: (a)  $\phi = 1.1$ , (b)  $\phi = 1.2$ , (c)  $\phi = 1.3$ .

of the parameter space. The use of free-slip conditions ( $\gamma = 0$ ) destabilizes the flow. Therefore, the stochastically induced regime transitions occur for smaller wind stress parameters  $\phi$ . In addition, the residence durations of the nonsymmetric regime for free-slip conditions are in general shorter than for half or no-slip boundary conditions.

## 2) INITIAL CONDITIONS

Several experiments are performed to test how the initial conditions change the behavior of the model. In

particular, the nonsymmetric high eddy energy state (Fig. 5b) is used as an initial condition for several runs with and without stochastic forcing; the use of the different initial conditions does not change the general results of the previous section. The model never stays in the nonsymmetric state longer than in the corresponding run starting from rest. Thus, the nonsymmetric state appears to be unstable. Furthermore, the mirror image of the nonsymmetric high eddy energy state (Fig. 5b) is alternatively used as an initial condition for several runs with and without stochastic forcing. The model immediately tends to the quasi-antisymmetric or the de-

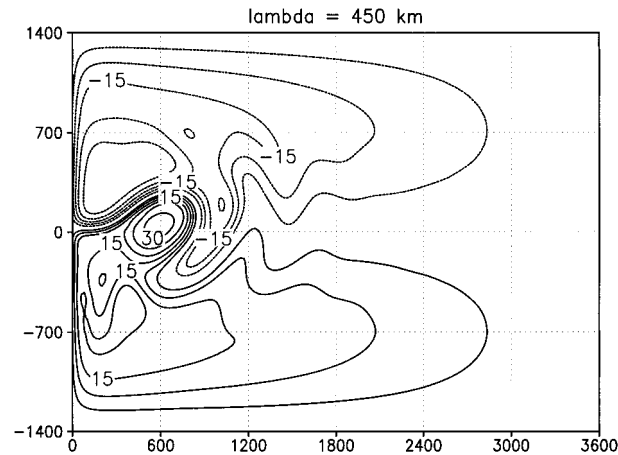


FIG. 10. Representative volume transport streamfunction field ( $10^6 \text{ m}^3 \text{ s}^{-1}$ ) for the high eddy energy state in a sensitivity experiment with a larger basin;  $\phi = 1$  and  $\lambda = 450 \text{ km}$ . The axes are horizontal distances in kilometers.

scribed nonsymmetric state; there is no evidence that the model resembles the mirror image of the nonsymmetric state under discussion.

### 3) BASIN SIZE

To test the robustness of the results to varying basin dimensions, several experiments are performed with the often used values of  $L_x = 3600 \text{ km}$  and  $L_y = 2800 \text{ km}$ . This domain is, for example, used by McCalpin and Haidvogel (1996) and Primeau (1998a). Three experiments with half-slip conditions are defined by the inhomogeneity parameters  $\lambda = 450, 900, \text{ and } 1800 \text{ km}$  ( $\lambda$  is chosen slightly larger because of the enhanced basin dimensions). The other parameters remain unchanged (Table 1). The use of the larger domain does not change the general results of the previous section. Again, the model shows a bimodal behavior that does not appear without the spatially inhomogeneous stochastic forcing. The nonsymmetric high eddy energy regime for the larger basin is presented in Fig. 10. Note that the nonsymmetric regime in Fig. 10 is qualitatively equal to the nonsymmetric regime in Fig. 5b.

### d. Summary

Although the regime behavior of the stochastically forced double-gyre system with increasing nonlinearity appears to be very complex with respect to the residence durations and the detailed transition probabilities of the two regimes, the results of the previously discussed experiments can be summarized in the following manner:

- The double-gyre model with a spatially inhomogeneous stochastic forcing shows a clear bimodal behavior in a highly nonlinear region of the parameter space. One regime shows a quasi-antisymmetric, the second regime a nonsymmetric flow pattern.

- It seems that the nonsymmetric regime corresponds to one member of a known nonsymmetric pair of stationary solutions found for larger basin dimensions.
- The nonsymmetric regime does not appear without the spatially inhomogeneous stochastic forcing nor with spatially homogeneous stochastic forcing. Thus, the regime transitions are induced by the spatial inhomogeneity of the white noise variance.
- The regime transitions commence from a positive curvature of the jet. After the transition the systems remains in the nonsymmetric regime for several years to decades before the northern extension of the anticyclonic recirculation gyre detaches, giving rise to the quasi-antisymmetric regime again.
- The occurrence of stochastically forced regime transitions does not depend sensitively on boundary conditions, initial conditions, and basin size.

Thus, the system undergoes a transition phenomenon, which can be called a “noise-induced transition” (Horsthemke and Lefever 1984). Noise-induced transitions can occur only if a certain amount of randomness is present in the environment of the system under consideration. More precisely, the system undergoes a characteristic qualitative change of its probability density function (PDF) due to the impact of the external noise. In the present case one observes that the qualitative structure of the PDF changes as a function of the spatial inhomogeneity of the stochastic forcing. This behavior of the system can be seen in a sequence of transient kinetic energy histograms (Fig. 11) estimating the PDF of the systems transient kinetic energy. For convenience, the experiments with the wind stress parameter  $\phi = 1.3$  and half-slip boundary conditions ( $\gamma = 0.5$ ) are chosen as an example, because the noise-induced transition is clearly seen (see Fig. 9 for the time series). The experiments with the nearly homogeneous and intermediate stochastic forcing ( $\lambda = 1200 \text{ and } 600 \text{ km}$ ) stay in the quasi-antisymmetric regime and never approach the nonsymmetric high eddy energy state with transient kinetic energies above  $3000 \text{ J m}^{-2}$ . The qualitative structure of the histogram changes as the stochastic forcing becomes spatially very inhomogeneous ( $\lambda = 300 \text{ km}$ ). The system to some extent occupies the nonsymmetric high eddy energy state above  $3000 \text{ J m}^{-2}$ . Because the variance of the nonsymmetric regime is very large the histogram does not show a peak but a plateau for the high eddy energy state.

## 4. Discussion

The simple wind-driven ocean model forced by a combination of a double-gyre wind stress and a spatially inhomogeneous stochastic field shows a bimodal behavior. One regime is a quasi-antisymmetric state with a free jet penetrating deep into the basin. A more or less strong meandering of the jet does not change the overall flow pattern of this regime. The second regime

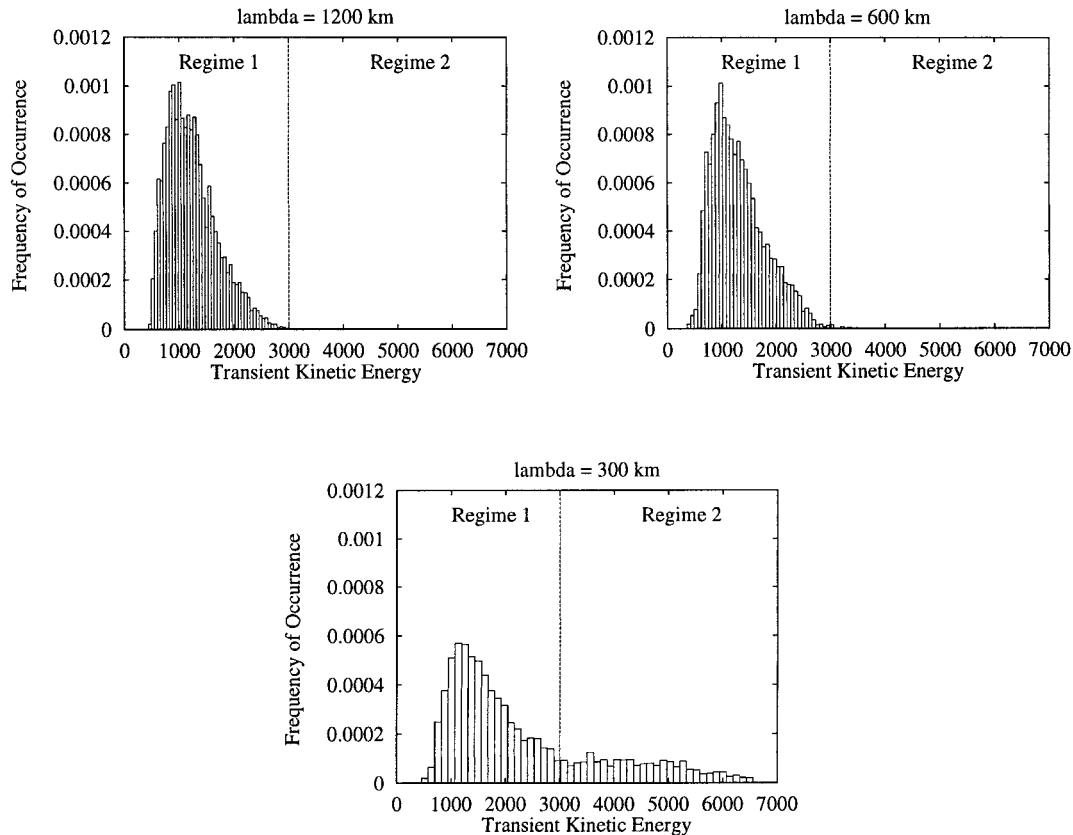


FIG. 11. Normalized histograms of transient kinetic energy ( $\text{J m}^{-2}$ ) for experiments with different inhomogeneity parameters  $\lambda = 1200, 600,$  and  $300$  km,  $\phi = 1.3$ ,  $L_x = L_y = 2400$  km, and half-slip boundary conditions ( $\gamma = 0.5$ ). The vertical line separating the quasi-antisymmetric (regime 1) and the nonsymmetric state (regime 2) visualizes the noise-induced transition.

appears to be related to the choice of the spatially inhomogeneous stochastic forcing. It consists of a nonsymmetric flow pattern with a very strong northern recirculation gyre and a northeastward flowing jet with a penetration scale of 500–600 km.

The unexpected result of the presented experimental setup is the appearance of the nonsymmetric regime in the presence of the spatially inhomogeneous stochastic wind forcing (Fig. 5b). This regime is found for boundary layer Reynolds numbers between  $\text{Re} \approx 1.86$  and  $\text{Re} \approx 2.76$ ; higher Reynolds numbers are not explored in this study. Furthermore, the stochastically forced regime transitions do not depend sensitively on boundary conditions, initial conditions, and basin size. It seems that the nonsymmetric regime corresponds to one member of a known nonsymmetric pair of stationary solutions that is found for larger basin dimensions, free-slip boundary conditions, biharmonic lateral diffusion, and boundary layer Reynolds numbers between  $\text{Re} \approx 0.4$  and  $\text{Re} \approx 1.8$  (Primeau 1998a) [Primeau (1998a) uses the same model configuration and parameters as McCalpin and Haidvogel (1996)]. This regime does not appear without the spatially inhomogeneous stochastic forcing. This is in agreement with McCalpin and Haid-

vogel (1996), who found no evidence for the nonsymmetric regime under discussion in the present paper. Nevertheless, McCalpin and Haidvogel (1996) show that the quasigeostrophic double-gyre model with a slightly asymmetric wind forcing appears to have several preferred regimes, which include a quasi-antisymmetric deeply penetrating state and a nonsymmetric weakly penetrating state; the bimodality is found for boundary layer Reynolds numbers between  $\text{Re} \approx 1$  and  $\text{Re} \approx 3$ . This behavior is recoverable using the primitive equations with steady antisymmetric wind forcing even with the smaller basin dimensions; it is observed within the present model configuration using free-slip boundary conditions. It is important to note that the nonsymmetric weakly penetrating state described by McCalpin and Haidvogel (1996), however, is clearly distinguishable from the nonsymmetric regime discussed in this paper. Therefore, it is expected that the stochastic forcing enables the system to reach the neighborhood of an unstable fixed point, which cannot be reached without the spatially inhomogeneous stochastic wind field. The unstable fixed point then acts to steer the model evolution in a temporarily persistent regime.

Although stationary solutions are not explicitly cal-

culated in this study, it appears to be reliable that the nonsymmetric regime is indeed an unstable stationary solution of the used model configuration. This notion is supported by the fact that the existence and the qualitative structure of the multiple double-gyre equilibria does not depend sensitively on the model configuration.

Therefore, stochastic perturbations are able to force transitions among multiple wind-driven oceanic flow regimes, at least for the particular stochastic forcing and the range of parameters explored in this study. The regime transitions into the nonsymmetric regime commence from an abnormally positive curvature of the jet. This structure is not attained without the spatially inhomogeneous stochastic wind stress. That is, the curl of the localized stochastic wind stress forces an anomaly that leads to the abnormal curvature of the jet. Thereby, the very small basin of attraction of the nonsymmetric state is reached and initiates the regime transition from the quasi-antisymmetric, low eddy energy state to the nonsymmetric, high eddy energy state. The transition back into the quasi-antisymmetric regime is caused by the detachment of the northern extension of the anticyclonic recirculation gyre. Although, the idealized stochastic forcing does not attempt to simulate observations, as well as the steady antisymmetric double-gyre wind stress, the spatially inhomogeneous stochastic forcing may serve as a useful conceptual tool to understand the effect of noise on simple wind-driven ocean models; adding a stochastic component to the steady wind stress makes the forcing more realistic and therefore more relevant to the real ocean.

Thus, the behavior of the wind-driven ocean circulation can be substantially modified by the stochastic forcing of the atmosphere. This emphasizes the important concept of noise-induced regime transitions in the wind-driven circulation. In this sense, the conjecture of Cessi and Ierley (1995) that multiple equilibria are of significance in the description of the low-frequency variability of the wind-driven ocean circulation, regardless of their stability, is supported.

*Acknowledgments.* During part of this work, PS enjoyed the hospitality of the CNR Istituto di Cosmogeofisica in Torino, Italy. We would like to thank Dr. Antonello Provenzale for many fruitful discussions. We thank one anonymous reviewer for valuable comments that led to improvements of the original manuscript. Furthermore, we appreciate the thoughtful comments of Dr. Francois Primeau. This work was supported by the European Science Foundation via the TAO Exchange Grant Program and the Deutsche Forschungsgemeinschaft within Sonderforschungsbereich 512.

#### REFERENCES

- Berloff, P., and S. P. Meacham, 1997: The dynamics of an equivalent barotropic model of the wind-driven circulation. *J. Mar. Res.*, **55**, 407–451.

- Cessi, P., and G. R. Ierley, 1995: Symmetry-breaking multiple equilibria in quasigeostrophic, wind-driven flow. *J. Phys. Oceanogr.*, **25**, 1196–1205.
- Dijkstra, H. A., and C. A. Katsman, 1997: Temporal variability of the wind-driven quasi-geostrophic double gyre ocean circulation: Basic bifurcation diagrams. *Geophys. Astrophys. Fluid Dyn.*, **85**, 195–232.
- Frankignoul, C., and K. Hasselmann, 1977: Stochastic climate models. Part II: Application to sea-surface temperature anomalies and thermocline variability. *Tellus*, **29**, 289–305.
- , and P. Müller, 1979: Quasi-geostrophic response of an infinite  $\beta$ -plane ocean to stochastic forcing by the atmosphere. *J. Phys. Oceanogr.*, **9**, 104–127.
- , —, and E. Zorita, 1997: A simple model of the decadal response of the ocean to stochastic wind forcing. *J. Phys. Oceanogr.*, **27**, 1533–1546.
- Haidvogel, D. B., J. C. McWilliams, and P. R. Gent, 1992: Boundary current separation in a quasigeostrophic, eddy-resolving ocean circulation model. *J. Phys. Oceanogr.*, **22**, 882–902.
- Hasselmann, K., 1976: Stochastic climate models. Part I. Theory. *Tellus*, **28**, 473–484.
- Horsthemke, W., and R. Lefever, 1984: *Noise-Induced Transitions: Theory and Applications in Physics, Chemistry, and Biology*. Springer-Verlag, 318 pp.
- Ierley, G. R., and V. A. Sheremet, 1995: Multiple solutions and advection-dominated flows in the wind-driven circulation. Part I: Slip. *J. Mar. Res.*, **53**, 703–737.
- Itoh, H., and M. Kimoto, 1996: Multiple attractors and chaotic itinerancy in a quasigeostrophic model with realistic topography: Implications for weather regimes and low-frequency variability. *J. Atmos. Sci.*, **53**, 2217–2231.
- , and —, 1997: Chaotic itinerancy with preferred transition routes appearing in an atmospheric model. *Physica D*, **109**, 274–292.
- Jiang, S., F.-F. Jin, and M. Ghil, 1995: Multiple equilibria, periodic and aperiodic solutions in a wind-driven, double-gyre, shallow-water model. *J. Phys. Oceanogr.*, **25**, 764–786.
- Kimoto, M., and M. Ghil, 1993a: Multiple flow regimes in the Northern Hemisphere winter. Part I: Methodology and hemispheric regimes. *J. Atmos. Sci.*, **50**, 2625–2643.
- , and —, 1993b: Multiple flow regimes in the Northern Hemisphere winter. Part II: Sectorial regimes and preferred transitions. *J. Atmos. Sci.*, **50**, 2645–2673.
- Legras, B., and M. Ghil, 1985: Persistent anomalies, blocking and variations in atmospheric predictability. *J. Atmos. Sci.*, **42**, 433–471.
- Marshall, J., and F. Molteni, 1993: Toward a dynamical understanding of planetary-scale flow regimes. *J. Atmos. Sci.*, **50**, 1792–1818.
- McCalpin, J., and D. B. Haidvogel, 1996: Phenomenology of the low-frequency variability in a reduced-gravity quasigeostrophic double-gyre model. *J. Phys. Oceanogr.*, **26**, 739–752.
- McClintock, P. V. E., 1999: Unsolved problems of noise. *Nature*, **40**, 23–24.
- Meacham, S. P., and P. Berloff, 1997: Barotropic, wind-driven circulation in a small basin. *J. Mar. Res.*, **55**, 523–563.
- Molteni, F., 1996a: On the dynamics of planetary flow regimes. Part I: The role of high-frequency transients. *J. Atmos. Sci.*, **53**, 1950–1971.
- , 1996b: On the dynamics of planetary flow regimes. Part II: Results from a hierarchy of orographically forced models. *J. Atmos. Sci.*, **53**, 1972–1992.
- Pedlosky, J., 1996: *Ocean Circulation Theory*. Springer-Verlag, 453 pp.
- Primeau, F. W., 1998a: Multiple equilibria and low-frequency variability of wind-driven ocean models. Ph.D. dissertation, Massachusetts Institute of Technology/Woods Hole Oceanographic Institution, 158 pp.
- , 1998b: Multiple equilibria of a double-gyre ocean model with super-slip boundary conditions. *J. Phys. Oceanogr.*, **28**, 2130–2147.
- Saravanan, R., and J. C. McWilliams, 1997: Stochasticity and spatial

- resonance in interdecadal climate fluctuations. *J. Climate*, **10**, 2299–2320.
- Scott, R. B., and D. N. Straub, 1998: Small viscosity behaviour of a homogeneous quasi-geostrophic, ocean circulation model. *J. Mar. Res.*, **56**, 1225–1258.
- Speich, S., H. Dijkstra, and M. Ghil, 1995: Successive bifurcations in a shallow-water model applied to the wind-driven circulation. *Nonlinear Processes Geophys.*, **2**, 241–268.
- Sura, P., F. Lunkeit, and K. Fraedrich, 2000: Decadal variability in a simplified wind-driven ocean model. *J. Phys. Oceanogr.*, **30**, 1917–1930.
- Wright, P. B., 1988: An atlas based on the COADS dataset: Fields of mean wind, cloudiness and humidity at the surface of the global ocean. Report No. 14, Max-Planck-Institut für Meteorologie, 68 pp. [Available from Max-Planck-Institut für Meteorologie, Bundesstrasse 55, D-20146 Hamburg, Germany.]